



Permittivity Estimation of Subsurface Deposits in the Elysium–Utopia Region on Mars with *MRO* Shallow Radar Sounder Data

Xu Meng¹ , Yi Xu¹ , Long Xiao^{1,2} , and Zhiyong Xiao^{1,3,4}

¹ State Key Laboratory of Lunar and Planetary Sciences, Macau University of Science and Technology, Macau, People's Republic of China; yixu@must.edu.mo

² State Key Laboratory of Geological Processes and Mineral Resources, Planetary Science Institute, School of Earth Sciences, China University of Geosciences, Wuhan 430074, People's Republic of China

³ Planetary Environmental and Astrobiological Laboratory, School of Atmospheric Sciences, Sun Yat-sen University, Zhuhai, People's Republic of China

⁴ CAS Center for Excellence in Comparative Planetology, Hefei, People's Republic of China

Received 2019 October 29; revised 2020 January 10; accepted 2020 February 3; published 2020 March 13

Abstract

Dielectric properties of the subsurface layers provide important clues to material compositions beneath the surface. The *Mars Reconnaissance Orbiter* (*MRO*) Shallow Radar (SHARAD) observed clear subsurface reflections in the Elysium–Utopia region, where morphological features such as impact craters with rampart ejecta suggest the possible presence of volatiles, but the permittivity of the subsurface unit beneath the surface strata has not been derived yet to provide independent evidence for or against the presence of water ice. In this paper, we employed a three-layer model consisting a surface mantling layer (layer I), a shallow subsurface layer (layer II), and a deep subsurface layer (layer III) to invert the permittivity of layer III, which considers the surface roughness and attenuation of radar waves in layer II. The obtained permittivity and loss tangent in the study region confirm that the materials of layer II are dense basaltic flows. Then, the permittivity of layer III is derived as 2.6 ± 0.9 , suggesting that subsurface water ice may be present, or a layer of dry and low-density deposits exists beneath the basalt layer. The hypothesis could be further tested by the ground-penetrating radar of China's first Martian mission, to be launched in 2020. Our results also show that the surface mantling layer included in the model is essential in the calculation of permittivity values.

Unified Astronomy Thesaurus concepts: Mars (1007); Martian satellites (1009); Radar astronomy (1329); Computational methods (1965)

1. Introduction

Radar sounders play an important role in characterizing the geological surface and subsurface features of Mars. They can transmit electromagnetic waves into the subsurface and record the reflected signals, which contain information from underground. The Mars Advanced Radar for Subsurface and Ionosphere Sounding (MARSIS) on ESA's *Mars Express* (Picardi et al. 2005) and the Shallow Radar (SHARAD) on *Mars Reconnaissance Orbiter* (Seu et al. 2007) have successfully revealed the subsurface structures and detected the existence of liquid or solid water below the Martian surface, such as polar layered deposits (Plaut et al. 2007; Selvens et al. 2010), shallow water ice deposits associated with debris-covered glaciers (Holt et al. 2008; Plaut et al. 2009), subsurface ice sheets (Bramson et al. 2015; Stuurman et al. 2016; Dundas et al. 2018), and pedestal craters (Nunes et al. 2011). Most of the observed ice and ice-rich deposits are close to the surface and they have been covered by a thin layer such as ice-cemented dust, regolith, and rock debris with a thickness of less than 20 m (Plaut et al. 2009; Dundas et al. 2018). Recently, permittivity derived from subsurface reflections indicates the presence of liquid water below the ice of the Martian South Polar Layered Deposits at a depth of ~ 1.5 km (Orosei et al. 2018). However, the search for liquid water buried in deep locations with a radar sounder is still in the first stage because of the limited observations and difficulties in estimating permittivity.

Vastitas Borealis Formation (VBF), located in the northern lowlands of Mars, is interpreted as a sedimentary deposit from the effluents of outflow channels (Kreslavsky & Head 2002). Clear subsurface reflections observed in SHARAD data have

been reported in the Elysium–Utopia region centered at $31^{\circ}2\text{N}$ $117^{\circ}6\text{E}$ (Figure 1) (Nunes et al. 2010), where extensive basaltic lava flows that erupted from the Elysium volcanic province covered the VBF unit located in the southern Utopia Planitia (Tanaka et al. 2005). Nunes et al. (2010) interpreted the radar reflectors as water ice near or at the surface based on the hydrovolcanic history of mega-lahars. However, subsequent studies estimate that the permittivity of the surface layer is between 6.5 and 9.5 (Nunes 2012a) and interpret that the reflections may be caused by the interface between the surface basalts and VBF (Nunes 2012b). Morphological features (impact craters with rampart ejecta and mud volcanism) in the Elysium–Utopia region indicate a high abundance of volatiles in the VBF materials in the past (Barlow 2006; Ivanov et al. 2014). However, the presence of water ice in the Elysium–Utopia region is still unclear because the permittivity of the subsurface VBF beneath the surface lava flows in this region has not yet been derived.

Previous studies used a two-layer model to estimate the permittivity of the subsurface layer by assuming that the surface layer is a low-loss medium (Lauro et al. 2010, 2012; Morgan et al. 2015). However, the surface layer in the Elysium–Utopia region is a high-loss lava flow and mantled by a thin layer of dust that is suggested to contribute to the radar observation of subsurface reflectors (Simon et al. 2014). In this paper, we establish a three-layer model consisting of the surface mantling layer (layer I), a shallow subsurface layer (layer II), and a deep subsurface layer (layer III) to estimate the permittivity of the deep subsurface layer. We find that the average permittivity value is 8.7 and the mean value of the loss tangent is 0.007, suggesting that the surface flows in the

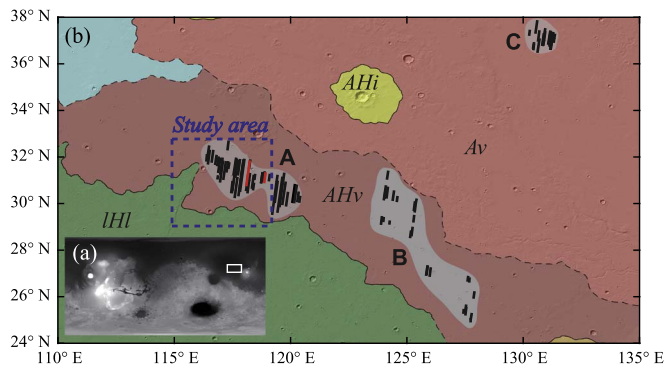


Figure 1. Mars Orbiter Laser Altimeter (MOLA) topography and geological map (Tanaka et al. 2014) of the Elysium–Utopia region. (a) Global elevation map showing the location of the Elysium–Utopia region; the white rectangle indicates the boundary of the main plate (b). (b) The locations of basal interfaces detected by SHARAD. Black and red straight lines indicate locations where SHARAD has detected subsurface reflections. The two red lines are radar observation tracks that have orbital numbers of 18228_01 (left) and 5095_01 (right).

Elysium–Utopia region are dense basalt. We estimate that the permittivity values of the deep subsurface VBF layer (layer III) are 2.6 ± 0.9 , markedly lower than the permittivity of rocks. Analysis of the composition of the VBF materials shows that water ice may be present within the VBF unit, or a layer of dry and low-density deposits lies between the lava flows and VBF.

This paper is organized as follows. Section 2 describes the SHARAD data used in the study area. In Section 3, the method for estimating permittivity of the deep subsurface layer is elaborated. In Section 4, the permittivity value of the deep subsurface unit is estimated and a detailed discussion of the VBF composition is given. Concluding remarks are given in Section 5.

2. Data Preparation

SHARAD is a radar sounder that transmits a linearly modulated pulse with a frequency of 15–25 MHz; one of its scientific objectives is to detect subsurface water and water ice on Mars (Seu et al. 2007). After synthetic aperture processing, SHARAD has a cross-track resolution of 3–6 km and an along-track resolution of 0.3–1 km (Seu et al. 2007). SHARAD is sensitive to off-nadir surface topographic features, so clutter simulation is necessary to distinguish real subsurface reflectors from the discrete reflectors caused by the off-nadir surface features. A secondary echo that is only visible in radargrams and does not occur in clutter simulation is considered to come from subsurface interfaces (Holt et al. 2006; Choudhary et al. 2016). The detection of subsurface interfaces is sensitive to several factors such as roughness, internal scattering, and dielectric properties of layers, which have been studied by many researchers over the years (e.g., Holt et al. 2008; Stillman & Grimm 2011; Simon et al. 2014).

We individually checked over 300 radargrams and found 69 of them showing clear subsurface reflections in the Elysium–Utopia region. Figure 1 shows the radar observation footprints of the subsurface reflectors indicated by the black and red straight lines. The observed reflectors are concentrated in three regions, named areas A, B, and C. Area C is located on the Amazonian volcanic unit and adjacent to terrains modified by water from or after lahars (Russell & Head 2003). Both areas A and B belong to the Amazonian and Hesperian volcanic unit. In

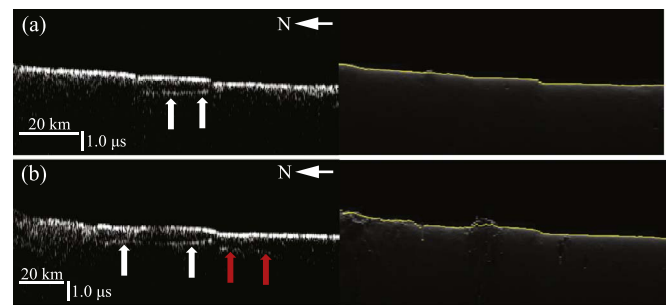


Figure 2. Subsurface reflectors in the Elysium–Utopia region. The orbit numbers of (a) and (b) are 5095_01 and 18228_01, which are indicated by red lines in Figure 1. The left part of the figure shows SHARAD radargrams and the right part corresponds to clutter simulation. Arrows denote subsurface reflectors that cannot be found in the cluttergrams.

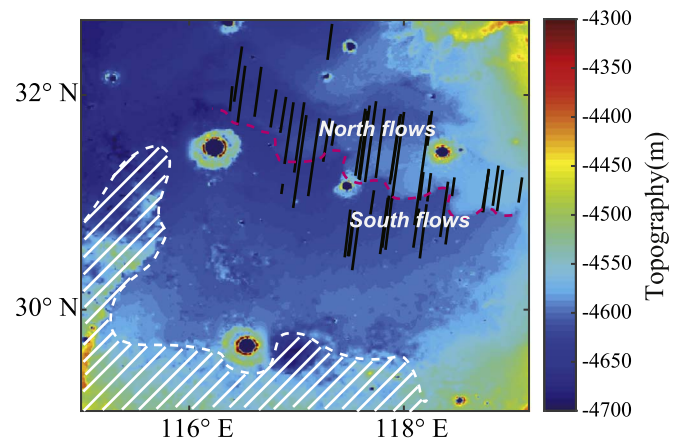


Figure 3. MOLA topography of the study area. The dashed pink line indicates the front of the lobate margin. The black lines are SHARAD subsurface reflectors which cross the lobate margin. Stripes denote the polygonal terrains. On the north side of the lobate front, we named the areas of high elevation where SHARAD detected subsurface reflectors as north flows. On the other side of the front, we named the areas of low elevation as south flows.

this paper, we mainly study area A because the depth of reflectors can be inferred from the topographic data. We did not find subsurface reflectors from MARSIS data, probably because the resolution of MARSIS in this region is ~ 50 m according to the dielectric map of the Martian northern hemisphere by Mouginot et al. (2012), which is larger than the maximum thickness of the surface flows.

Figure 2 gives two examples of radar reflectors. Figure 2(a) shows a single subsurface reflector that gradually extends to the surface. The entire right reflector (red arrows) in Figure 2(b) is totally underground whereas the left reflector (white arrows) also extends to the surface, similar to Figure 2(a). In the topographic image shown in Figure 3, the SHARAD footprints cross the lobate margin, which is the boundary between north flows and south flows. The north flows are younger than the south ones because they lie on top of them. Most of the reflections appear around the lobate margin and nearly half of radargrams show subsurface echoes in the south flow region. Based on the geological map (Tanaka et al. 2014) and our speculation, the white arrows (Figure 2) indicate the interface between the north and south flows, whereas the red arrows indicate a deeper subsurface interface beneath the south flows.

3. Methodology

3.1. Estimation of Permittivity of Shallow Materials

With the time delay and estimated depth of reflectors between the north flows and south flows, we can calculate the relative permittivity ϵ' of the surface flows based on the equation

$$\epsilon' = \left(\frac{c\tau}{2h} \right)^2 \quad (1)$$

where c is the speed of light in free space, h is the layer thickness, and τ is the round-trip travel time delay between the surface and subsurface echoes measured from the radargrams.

Radar processing software, Reflexw (Sandmeier 2012), is used to trace the surface and subsurface echoes and generate the time delay (τ). According to the Mars Orbiter Laser Altimeter (MOLA) topography of the study area, the north flows lie on top of the south flows, hence the thickness (h) of the north flows is equal to the difference in surface elevation between the north and south flows. Note that the MOLA topography shows that the surface of the south flows is not flat and rises from north to south (Figure 3). Therefore, the thickness of the north flows is inferred based on an extrapolation of the surface of the south flow dipping beneath the north flow.

3.2. Estimation of Loss Tangent of Shallow Materials

The loss tangent derived from the power loss between the surface and subsurface echoes can be used to analyze the electrical properties of Martian materials (Campbell et al. 2008). When computing the loss tangent ($\tan \delta$), we assume that the surface roughness would not affect the mean rate of decay of subsurface power with depth. Following the method proposed by Porcello et al. (1974) and Orosei et al. (2017), the surface echo power P_s and subsurface echo power P_{ss} can be expressed as follows:

$$P_s = P_t \left(\frac{G\lambda}{8\pi H} \right)^2 |R_s|^2 L_s \quad (2)$$

$$P_{ss} = P_t \left(\frac{G\lambda}{8\pi(H+z)} \right)^2 (1 - |R_s|^2)^2 |R_{ss}|^2 \times \exp(-2\pi f \tan \delta \tau) L_{ss} \quad (3)$$

where P_t is the transmitted power, G is the antenna gain, λ is the wavelength, H is the spacecraft altitude, z is the layer thickness, f is the radar frequency, R_s is the surface reflection coefficient, R_{ss} is the subsurface reflection coefficient, L_s and L_{ss} are the generic roughness loss terms at the surface and subsurface interfaces, and τ has been defined in Equation (1). By taking the natural logarithm of Equation (3) divided by Equation (2), the following term is obtained:

$$\ln \left(\frac{P_{ss}}{P_s} \right) = -2\pi f \tau \tan \delta + K. \quad (4)$$

In Equation (4), $\tan \delta$ depends only on the slope of $\ln(P_{ss}/P_s)$ versus $2\pi f \tau$. The constant term K is determined by the reflection coefficients and roughness losses at the subsurface and surface interfaces.

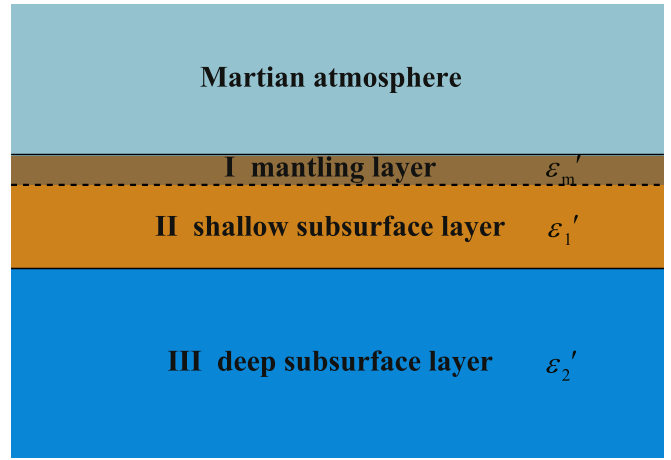


Figure 4. Model for estimating the permittivity of the deep subsurface layer.

3.3. Estimation of Permittivity of the Deep Subsurface Layer

In Equation (4), the constant term K is dependent on the surface and subsurface reflection coefficients, which are related to the permittivity of the layers and the roughness losses. If the permittivity of the surface layer is known, we could estimate that of the subsurface layer based on the corrected values (K') of K , in which the influences of roughness losses are neglected. In this paper, we establish a three-layer model, which is composed of the mantling layer (containing eolian sand, dust, and regolith), the shallow subsurface layer, and the deep subsurface layer (from top to bottom), to invert the radar observation in the study area (Figure 4). Previous studies suggest that the low-density mantling layer would substantially improve the radar penetration into the buried flows (Carter et al. 2009; Simon et al. 2014). There is evidence supporting the existence of the mantling layer and that the thickness of the layer will affect the strength of the surface echo of SHARAD.

The *Viking* landers revealed that fine-grained sediment and dust cover the surface of Mars (Arvidson et al. 1989). The thickness of the mantling layer on Mars is non-uniform and constrained locally by various factors, such as exposure age, impact production rate, frequency distribution of crater size, geological processes (e.g., sedimentary deposition and eolian erosion), and additional surface erosion (e.g., wind) (Warner et al. 2017). Remote sensing approaches can obtain the global coverage of the mantling materials. For example, emissivity spectra from the *Mars Global Surveyor* Thermal Emission Spectrometer (MGS-TES) and Earth-based radar images show that dust appears widely on the surface of Mars, such as in Tharsis, Arabia Terra, and Elysium areas including our study region (Ruff & Christensen 2002; Harmon et al. 2012; Ody et al. 2014). However, due to limited probing depth, the thickness of the mantling layer still cannot be determined. Maps of surface permittivity produced using surface reflections of the radar sounder also give hints of the existence and the thickness of the mantling layer. For instance, in the study region, a permittivity value of 9.3 ± 1.0 is inferred from MARSIS and a low permittivity value of 3–4 is inferred from SHARAD (Mouginot et al. 2012; Castaldo et al. 2017). The mismatch is due to the different probing depths of MARSIS and SHARAD, the values of which represent the dielectric properties of the first 60–80 m and the first few meters, respectively. The disagreement between the results of MARSIS and SHARAD supports the proposed three-layer model. The

low value from SHARAD suggests that the surface in the study region is composed of low-density materials (Castaldo et al. 2017). The existence of the mantling layer is invisible at the resolution of SHARAD, but can improve the power of subsurface echoes.

Note that the surface mantling layer is only considered for the estimation of dielectric properties in the regions where its thickness reaches the order of one meter, which can be inferred with the permittivity map when the result from SHARAD is lower than that from MARSIS and with other geological evidence, e.g., crater morphology (Mangold et al. 2009; Warner et al. 2017) and observations from a lander/rover (Grant et al. 2004; Golombek et al. 2006).

On Mars, there is not much information about the dielectric properties of the mantling layer in the absence of returned samples. Laboratory measurements of the JSC Mars-1 Martian soil simulant show that the relative permittivity is mostly between 2.5 and 3.0 at the SHARAD frequency (Brouet et al. 2019). Regolith samples from *Apollo* missions have average relative permittivity values of ~ 3 (Carrier 1991). A map of surface permittivity from SHARAD data reveals 3–4 for the permittivity of the first few meters in the study region (Castaldo et al. 2017). In this paper, we choose 3.0 ± 0.5 as the permittivity of the mantling layer.

The transmissivity of radar waves between the mantling and the shallow subsurface layers is assumed to be 1 because the thickness (less than a few meters) of the mantling layer is less than the SHARAD wavelength (for further discussion see the Appendix). According to Figure 4, surface reflections are caused by the interface between the mantling layer and free space. The surface reflection coefficient at normal incident is

$$R_s = \frac{1 - \sqrt{\epsilon'_m}}{1 + \sqrt{\epsilon'_m}} \quad (5)$$

with ϵ'_m being the permittivity of the mantling layer.

The subsurface reflections are from the interface between layers II and III. So, the reflection coefficient at the subsurface interface is

$$R_{ss} = \frac{\sqrt{\epsilon'_2} - \sqrt{\epsilon'_1}}{\sqrt{\epsilon'_2} + \sqrt{\epsilon'_1}} \quad (6)$$

where ϵ'_1 and ϵ'_2 are the relative permittivities of layers I and II, respectively. By substituting Equations (5) and (6) into Equations (2) and (3) respectively, the expression for K in Equation (4) becomes

$$K = \ln \left[\frac{(1 - |R_s|^2)^2 |R_{ss}|^2 L_{ss}}{|R_s|^2 L_s} \right] \quad (7)$$

where the influences of roughness losses can be neglected after the correction of K (for more details see Section 4.3), so Equation (7) is simplified as

$$K' = \ln \frac{(1 - |R_s|^2)^2 |R_{ss}|^2}{|R_s|^2}. \quad (8)$$

K' , the left side of Equation (8), is the corrected value of K in Equation (4), whereas the right side depends on the permittivity values of the three-layer model. Based on previous studies, the permittivity (ϵ'_m) of the mantling layer lies in the range 2.5–3.5. The permittivity (ϵ'_1) of layer II is obtained from Equation (1).

Table 1
Permittivity Values and Error where Appropriate for Each of the Flows Detected in the Elysium–Utopia Region

Track Number	Permittivity (ϵ')	1σ Error on Permittivity
4950_01	8.2	1.44
5095_01	7.4	1.24
5161_01	10.6	1.77
5517_01	8.4	2.35
5662_02	8.2	1.16
5939_02	8.7	1.62
12848_01	10.2	2.72
13059_01	8.4	2.33
13626_01	8.4	1.44
18228_01	7.7	1.50
20496_01	8.3	1.33
20707_01	8.6	1.41
21775_01	9.1	1.77
24109_01	8.0	1.84
24386_01	8.3	1.49
24531_01	9.3	1.58
25098_01	9.3	1.07
25520_01	9.0	2.05
25731_01	10.0	2.28
26298_02	8.0	2.42

Therefore, the permittivity (ϵ'_2) of layer III can be estimated from Equation (8).

In the algorithm, reflection coefficients are obtained by assuming that electromagnetic waves propagate into a smooth interface at normal incidence. The influence of material inhomogeneities within the subsurface deposits on the scale of the SHARAD wavelength would result in volume scattering and lead to a systematic overestimation of $\tan \delta$ (Orosei et al. 2017). Therefore, we use the pulse width as an effective index for surface and subsurface roughness in the estimation of the permittivity of layer III (details in Section 4.3), which also reduces most of the effects of volume scattering (Lauro et al. 2012).

4. Results

4.1. Permittivity and Loss Tangent of Layers I and II

Based on Equation (1), we calculated that the permittivity values of materials between the surface and the subsurface reflectors range from 7.4 to 10.6 (Table 1), with a mean of 8.7 and a standard deviation of 0.8. The uncertainties introduced in the processing of permittivity mainly come from the measurement of layer thicknesses and the travel time delay (Simon et al. 2014). The permittivity value of 8.7 is consistent with basaltic flows because most terrestrial and lunar basalts have ϵ' values between 7 and 11 (Carrier 1991). Therefore, we interpret the surface materials as dense basalt. A linear regression is applied to compute the values of loss tangents (Orosei et al. 2017) for eight subsurface reflections in the Elysium–Utopia region (Table 2). Examples of tracks 4950_01 and 25520_01 are shown in Figure 5. The values of loss tangent range from 0.0055 to 0.0085, with an average of 0.007 (Table 2). For other subsurface reflections, we were unable to derive meaningful loss tangents because the round-trip travel times of the subsurface reflections do not show a wide distribution.

In the study region, SHARAD detected the bottom of the young north flow and a deeper subsurface reflector after the end of this flow. Context Camera (CTX) images and similar values

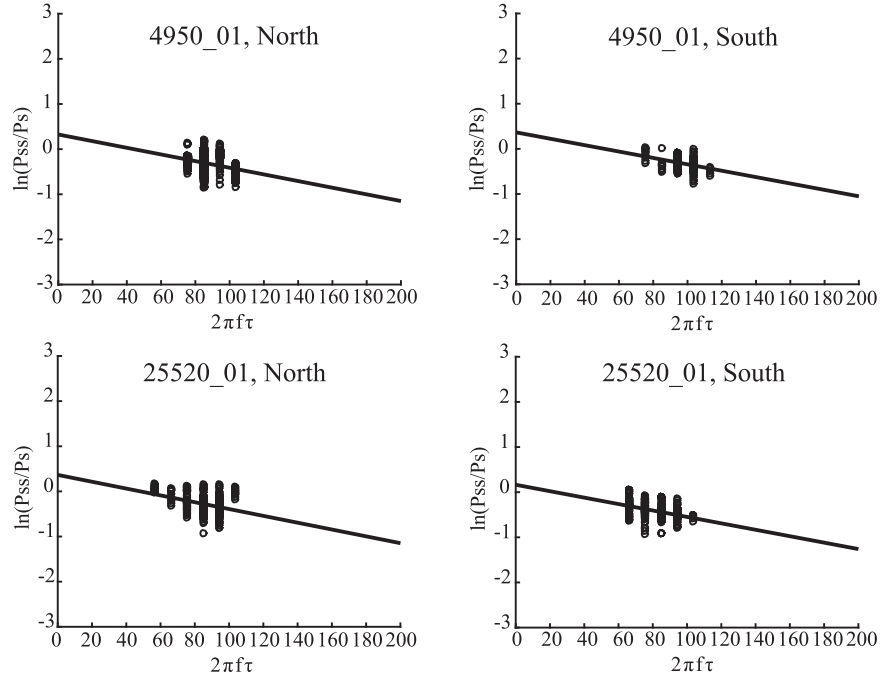


Figure 5. Plot of the natural logarithm of the ratio of subsurface to surface echo power vs. the number of cycles completed by the radar wave within the Elysium-Utopia region. The best fit lines are computed by using a linear regression.

Table 2

Coefficients of the Best Fit Lines for Loss Tangent, Together with Their 95% Confidence Bounds

Area	Track Number	Loss Tangent and the 95% Confidence Interval	Constant Term (K) and the 95% Confidence Interval
North	4950_01	0.0074 [0.0057, 0.0090]	0.3243 [0.1829, 0.4657]
	25520_01	0.0076 [0.0057, 0.0095]	0.3651 [0.2001, 0.5300]
	26298_02	0.0085 [0.0062, 0.0107]	0.3757 [0.2113, 0.5400]
South	4950_01	0.0071 [0.0048, 0.0092]	0.3656 [0.1432, 0.5880]
	20707_01	0.0055 [0.0041, 0.0069]	0.0869 [-0.0587, 0.2324]
	23542_01	0.0065 [0.0048, 0.0082]	0.3568 [0.1894, 0.5242]
	24531_01	0.0063 [0.0044, 0.0082]	0.3322 [0.1392, 0.5251]
	25520_01	0.0071 [0.0052, 0.0091]	0.1642 [0.0043, 0.3242]

of loss tangent (Table 2) reveal that the surface materials of both the north and south flows are basaltic lava (Russell & Head 2003; Tanaka et al. 2005). The reflections in the north flows (Figure 3) indicate the interface between lava flows that erupted in different periods, which is similar to the stratigraphy of the Tharsis region (Simon et al. 2014) and Elysium Planitia (Morgan et al. 2015). The subsurface reflection under the north flows may be caused by the mantling layer formed by the erosion of the second basalt layer, although a volatile-rich dust layer formed during an Amazonian high-obliquity period cannot be ruled out (Head et al. 2003).

4.2. Correction of Permittivity of Layer II

In Section 4.1, we calculated the permittivity of the substance between the surface and the subsurface reflectors. According to our model (Figure 4), the value of $\epsilon' = 8.7 \pm 0.8$ corresponds to a combined result from radar waves in layer I and layer II. By converting time to distance, Equation (1) is reformulated as

$$\epsilon' = \left(\frac{c\tau}{2h}\right)^2 = \left(\frac{\hat{h}}{h}\right)^2 \quad (9)$$

where \hat{h} is the apparent thickness of the subsurface reflectors, which is obtained from the time delay by assuming unitary permittivity. We obtain

$$\hat{h} = h\sqrt{\epsilon'} \quad (10)$$

with $\epsilon' = 8.7 \pm 0.8$. Based on the three-layer model in Figure 4, the apparent depth of layer II is expressed as

$$\hat{h}_1 = h\sqrt{\epsilon'} - h_m\sqrt{\epsilon'_m}. \quad (11)$$

By substituting Equation (11) into (9), the permittivity of layer II should be computed as

$$\epsilon'_1 = \left(\frac{h\sqrt{\epsilon'} - h_m\sqrt{\epsilon'_m}}{h - h_m}\right)^2 \quad (12)$$

where h_m is the thickness of layer I.

Equation (12) suggests that the estimated ϵ'_1 is dependent on the values of h and h_m . In the study area, most of the subsurface reflections have round-trip travel times of 600–900 ns, corresponding to a thickness between 30 and 46 m. The thickness of the mantling layer is estimated to be in the range of 1–10 m.

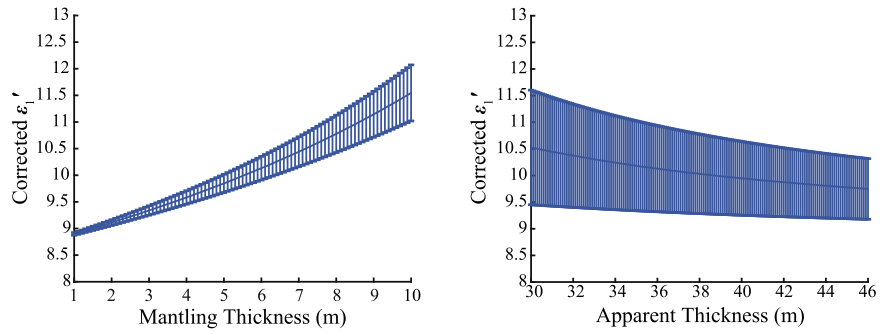


Figure 6. Estimated results based on Equation (12). Plots are computed based on $\epsilon' = 8.7$ and $\epsilon'_m = 3.0$.

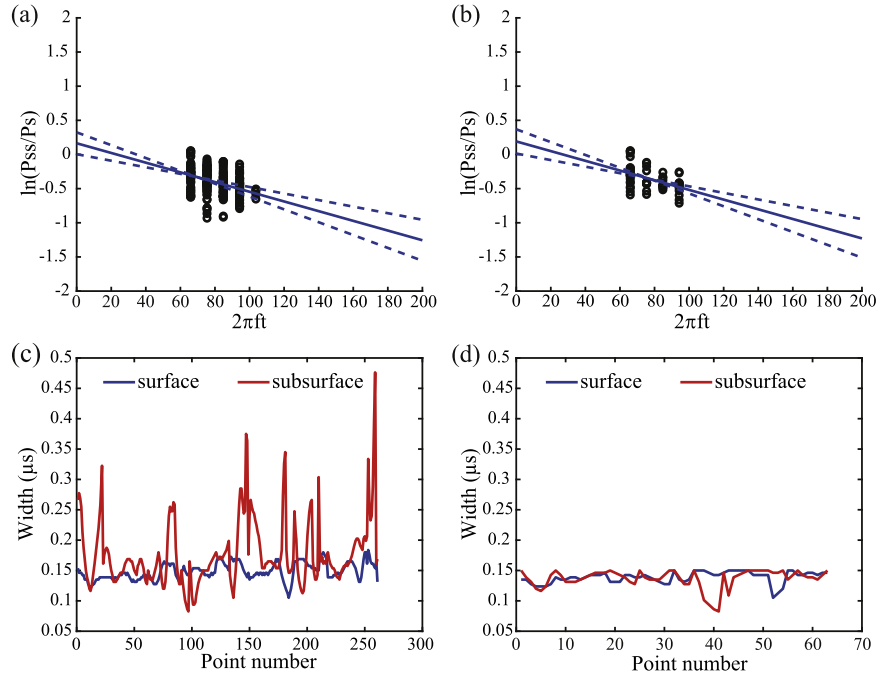


Figure 7. Example of correction of the constant term (25520_01, south). (a) Ratio of subsurface to surface echo power vs. the number of cycles before correction. (b) Ratio of subsurface to surface echo power vs. the number of cycles after correction. (c) Width of the reflections used in (a) at -3 dB with respect to the maximum. (d) Width of the reflections used in (b) at -3 dB with respect to the maximum.

Figure 6 shows an example of the corrected results for the permittivity of layer II by considering values for h and h_m . It is important to note that the corrected permittivity of layer II is mainly dominated by the mantling thickness. The corrected values and its errors increase with the mantling thickness. The corrected values are ~ 9 when the mantling layer is thin, but change to 12 when the mantling thickness is 10 m. By considering the mantling permittivity of 3.0 ± 0.5 , we compute that the average permittivity of layer II is 10.1 with a standard deviation of 0.8. Finally, we use $\epsilon'_1 = 10.1 \pm 0.8$ as the permittivity of layer II in the estimation of deep subsurface permittivity.

4.3. Correction of the Constant Term

In Equation (7), the constant term (K) is complicated by the roughness losses at the surface and subsurface interfaces. The values of K in Table 2 cannot be directly used to estimate the permittivity of layer III. In principle, the roughness losses (L_s and L_{ss}) could be evaluated from the roughness at the interfaces (Haynes et al. 2018). Such an evaluation would

require elevation data with a lateral resolution of about 1/10 of the SHARAD's 15 m wavelength (Ulaby et al. 1986); however, MOLA data have a spatial resolution of ~ 400 m (Smith et al. 2001), and no other high-resolution Digital Elevation Model (DEM) data are available in the study area.

Therefore, we use the following method to correct the constant term by considering the influences of roughness based on two principles: (1) loss tangent is independent of the reflection coefficients and the roughness (Equation (4)); (2) reflections whose pulse width at -3 dB with respect to the maximum is smaller than $0.15 \mu\text{s}$ are less affected by the roughness (Lauro et al. 2012). The method is described below.

First, pick clear subsurface reflections and their corresponding surface reflections. Then, compute the loss tangent that is equal to the slope of the best fit line of $\ln(P_{ss}/P_s)$ versus $2\pi f\tau$, while the initial constant term is the intercept of the best fit line and the y axis (Figure 7(a)).

Second, the widths of the surface and subsurface reflections at -3 dB with respect to the maximum are calculated (Figure 7(c)). To identify smooth portions in the study area,

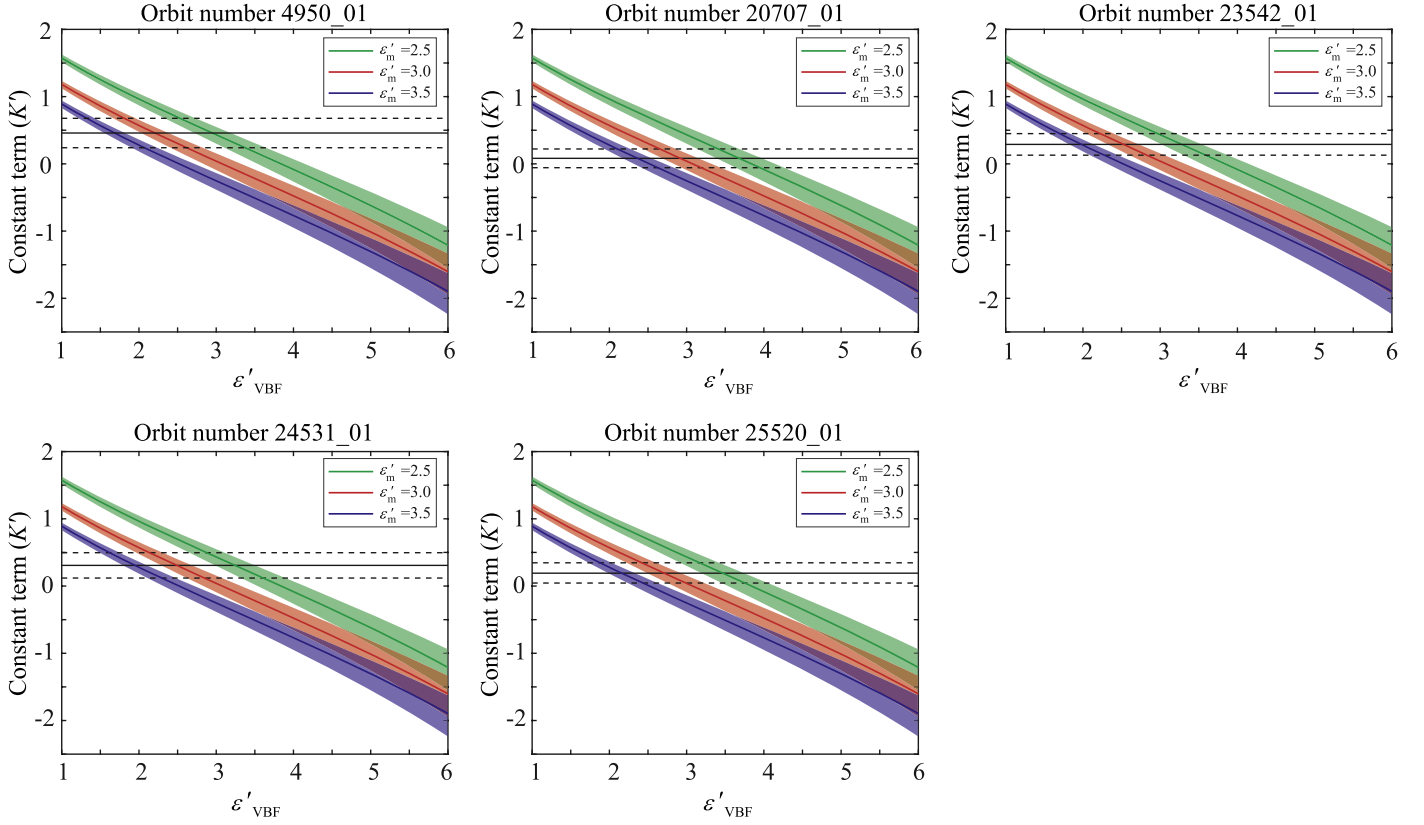


Figure 8. The estimated relative permittivity values of VBF from the constant term K' . The black and dashed black lines stand for the constant term and its 95% confidence interval. The green, red, and blue bars show the computed values of K' based on $\epsilon'_m = 2.5$, $\epsilon'_m = 3.0$, and $\epsilon'_m = 3.5$, respectively.

Table 3

Corrections of the Constant Term, Together with Their 95% Confidence Bounds

Area	Track Number	Constant Term and 95% Confidence Interval	
		Before Correction (K)	After Correction (K')
South flows	4950_01	0.3656 [0.1432, 0.5880]	0.4586 [0.2398, 0.6774]
	20707_01	0.0869 [-0.0587, 0.2324]	0.0820 [-0.0572, 0.2213]
	23542_01	0.3568 [0.1894, 0.5242]	0.2894 [0.1291, 0.4496]
	24531_01	0.3322 [0.1392, 0.5251]	0.3073 [0.1190, 0.4957]
	25520_01	0.1642 [0.0043, 0.3242]	0.1913 [0.0447, 0.3457]

we select only those reflections whose pulse widths are smaller than $0.15 \mu\text{s}$ (Figure 7(d)).

Third, use the loss tangent obtained from the first step as the slope value and obtain the corrected constant term with selected reflections (Figure 7(b)).

Figure 7 shows an example of the correction after taking consideration of roughness. The value increases from 0.164 to 0.191 (blue lines in Figures 7(a) and (b)). Table 3 lists the corrected values (K') of the constant term and their initial values (K). The maximum difference between the corrected and initial values is ~ 0.1 , which would cause a change of ~ 0.2 in the estimated permittivity values of the deep subsurface layer.

4.4. Permittivity of Layer III

The reflectors in the south flows are interpreted as the interface between the southern lava flows and the VBF unit. By assuming that the northern and southern lava flows in the study area have the same value of permittivity, we estimate the permittivity of the underlying VBF unit by using the method described in Section 3. The geological model is composed of a mantling layer, lava flows, and VBF materials (top to bottom). By applying the three-layer model to characterize the corrected constant term in Table 3, we calculate the permittivity of VBF beneath the lava flows. Previous studies suggest that VBF materials are sediments of low or moderate density (Campbell et al. 2008; Mouginot et al. 2012), so the range of potential relative permittivity of VBF is limited to between 1 and 6. In the estimation, the permittivity values of layer I and layer II are 3.0 ± 0.5 and 10.1 ± 0.8 , respectively.

The intersections of the color bars and black lines in Figure 8 show the inverted permittivity values of VBF, which are listed in Table 4. Note that the reason why K' in Figure 8 ranges from positive to negative is because that K' is in the logarithmic domain. When the subsurface reflection coefficient R_{ss} is larger than $R_s/(1 - |R_s|^2)$, the constant term K' is positive. Otherwise, K' is negative. For $\epsilon'_m = 3.0$, the VBF materials have a relative permittivity value of 2.6 ± 0.3 to satisfy the SHARAD observations. If considering the 95% confidence interval of the constant term K' and the uncertainty of the permittivity of the mantling layer, the value of ϵ'_{VBF} ranges from 1.67 to 3.44. When the relative permittivity of the mantling layer reduces to 2.5, the inverted value of ϵ'_{VBF} is 3.3 ± 0.4 with a 95% confidence interval of 2.33–4.26. If the

Table 4

Estimation of Relative Permittivity from the Constant Term, Together with Its 95% Confidence Bounds

Area	Track Number	Relative Permittivity of the VBF Based on		
		$\epsilon'_m = 2.5$	$\epsilon'_m = 3.0$	$\epsilon'_m = 3.5$
South Flows	4950_01	2.9 [2.33, 3.64]	2.2 [1.67, 2.82]	1.7 [1.21, 2.23]
	20707_01	3.7 [3.14, 4.26]	2.9 [2.43, 3.44]	2.4 [1.94, 2.83]
	23542_01	3.3 [2.73, 3.88]	2.5 [2.05, 3.05]	2.0 [1.56, 2.46]
	24531_01	3.2 [2.65, 3.90]	2.5 [1.97, 3.07]	1.9 [1.49, 2.48]
	25520_01	3.5 [2.92, 4.06]	2.7 [2.22, 3.23]	2.2 [1.73, 2.63]

mantling layer has a higher ϵ'_m value of 3.5, the relative permittivity of VBF materials is estimated to be 2.0 ± 0.3 . The 95% confidence interval is between 1.21 and 2.83 (Table 4).

From the results, we can observe that different permittivity values of the mantling layer all yield a low permittivity of layer III, indicating a low-density material. Also, the permittivity of deep subsurface VBF materials has an inverse relationship with that of the mantling layer. If removing the mantling layer, based on Equation (8), the deep subsurface VBF materials need to have relative permittivity of <1.0 to satisfy the constant term (K') in Table 3, which is unphysical for normal materials. Based on different permittivity values of the mantling layer, we use the derived 2.6 ± 0.9 as the relative permittivity of VBF.

4.5. Discussions

Lava flows in the Tharsis region have ϵ' values ranging from 7.6 to 11.6, with an average of 9.6, and the mean value of $\tan \delta$ ranges from 0.0078 to 0.029 with an average of 0.01 (Carter et al. 2009; Simon et al. 2014). In Elysium Planitia, SHARAD data were fit to obtain $\epsilon' = 8.8 \pm 1.0$ (Stillman & Grimm 2011), and a $\tan \delta$ value of 0.022 ± 0.011 (Campbell & Morgan 2018). Our results of $\epsilon' = 8.7 \pm 0.8$ and $\tan \delta = 0.007 \pm 0.0015$ are slightly lower than those for the Tharsis region and Elysium Planitia. Our low values may be caused by the surface mantling layer or porosity within the basaltic lava flows. Dust has covered the surface of the three mentioned regions (Ruff & Christensen 2002; Ody et al. 2014), but Earth-based radar measurements of these regions show similar brightness (Harmon et al. 2012), which means no clear difference in the thickness of the dust layer. The resurfacing of the Elysium–Utopia region occurred between 1.66 Ga and 3.08 Ga (Werner 2009; Werner et al. 2011), whereas the age of the Tharsis region is hundreds of million years and Elysium Planitia is the youngest volcanic plain on Mars (Vaucher et al. 2009). Generally, the aged surface of the Elysium–Utopia region experiences more impact events and a longer time of erosion, which could have contributed to the relatively thick mantling materials and thus the low value of ϵ' and $\tan \delta$.

In the study region, we derived $\epsilon' = 8.7 \pm 0.8$ for materials in the first ~ 40 m including the mantling layer and the lava flows. Our results are consistent with the MARSIS observation (9.3 ± 1.0) in the Elysium rise unit because the probing depth of MARSIS is close to the total thickness of the mantling and lava layers and is less affected by the deep subsurface layer with low permittivity (Mouginot et al. 2010). In Utopia

Planitia, the permittivity value derived with MARSIS data is 4.5 ± 1.0 and it is 3–4 with SHARAD data, indicating that the VBF unit may have a porosity of 35% or a content of water ice within the first tens of meters (Mouginot et al. 2012; Castaldo et al. 2017). In this paper, the permittivity of the deep subsurface VBF unit is estimated to be 2.6 ± 0.9 , agreeing with the lower end of the range of permittivity derived by SHARAD and MARSIS in Utopia Planitia.

$\epsilon'_{\text{VBF}} = 2.6 \pm 0.9$ is markedly lower than the permittivity of rocks. One possibility is the presence of a soil deposit composed of ice-poor and low-density materials between the lava flows and VBF unit. In our study region, the thickness of the south flows mostly ranges from 34 to 44 m, with an average of ~ 40 m. According to compaction studies of Martian materials (Watters et al. 2017), the relative permittivities of loose sand, volcanic ash, and silicate dust at a depth of 40 m are ~ 1.6 , 1.9, and 2.7, respectively. These values are consistent with the low end of our estimated results ($\epsilon'_{\text{VBF}} = 2.6 \pm 0.9$), which means that a buried layer of soil deposit can cause the subsurface reflections as in Elysium Planitia (Morgan et al. 2015).

Another possibility is that excess ice exists in the underlying VBF unit or the top few meters of VBF. The origin of VBF is interpreted as the effluent of outflow channels, and the ice-rich deposits were believed to sublimate and be lost in a short geological time if an insulating layer did not form rapidly (Kreslavsky & Head 2002). In the central portion of Utopia Planitia, mud volcanism and the morphology of impact craters with pancake-like ejecta provide the evidence for the existence of an ancient large body of water (Ivanov et al. 2014). The impacts occurred later than the resurfacing events, so the volatiles come from the layer beneath the lava flows. Moreover, polygonal terrains are located on the surface of the VBF unit that is adjacent to the south flows (Figure 3). The elevation of the south flows is lower than that of the polygonal terrains, which means the VBF unit beneath lava flows might be related to water or ice in the past. Etched flows were also found on the surface of south lava flows. Ivanov et al. (2014, 2015) interpreted the etched flows as the results of the eruption of mud and suggested the presence of a water or ice-related reservoir within the VBF unit.

We assume the VBF consists of water ice ($\epsilon' = 3.15$), lithic material with a relative permittivity of 10 (a value consistent with that of the lava flows, see Section 4.2), and pore space as the sedimentary deposits of the effluents of the outflow channels (Kreslavsky & Head 2002). By following the three-phase power relation from Stillman et al. (2010), Figure 9 shows the potential composition of deposited material. The surface porosity of Martian loose wind drift material is $\sim 50\%$ from the measurements taken at the *Viking* landing sites (Moore et al. 1987). Therefore, we adopt the value of 50% as the upper limit for the porosity of the VBF unit. In this paper, the estimated relative permittivity of the VBF materials ranges from 1.7 to 3.5 with an average of 2.6. It is infeasible to find any three-phase combination of depositions at the low end of $\epsilon'_{\text{VBF}} = 1.7$ because the contour line is inside the implausible corner (Figure 9). For the high end of $\epsilon'_{\text{VBF}} = 3.5$, the value is close to that of pure water ice. A relative permittivity of ~ 1.9 is the lowest value for a porosity less than 50%, where no rock fraction is contained. The volume fraction of ice is larger than 10% for a relative permittivity of 1.9–3.5.

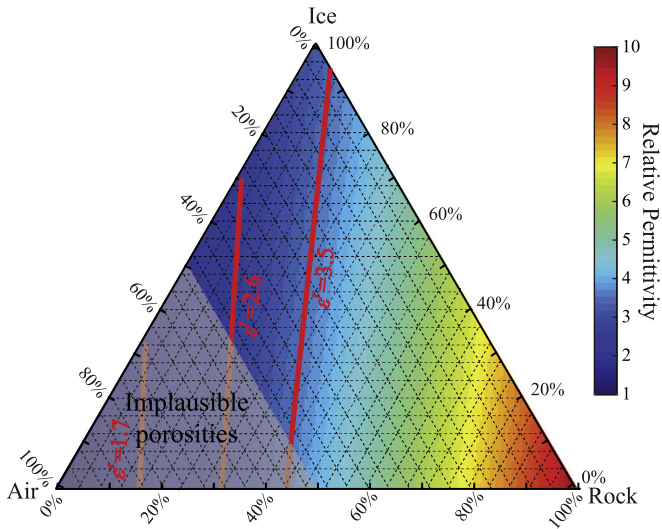


Figure 9. Ternary diagram of relative permittivity calculations for a mixture of ice, rock, and air. Porosities greater than 50% are considered implausible (Moore et al. 1987). The red lines represent the contours for three relative permittivity values of 1.7, 2.6, and 3.5.

The water ice in the VBF may be from atmospherically deposited H_2O as in the western Utopia Planitia (Stuurman et al. 2016) or the sublimation residue from frozen bodies of water (Kreslavsky & Head 2002). On Earth, a buried glacial ice layer beneath a thin granite drift has most likely not been active since 8.1 Ma, even though the distance between the ground surface and buried ice is from 25 to 80 cm (Marchant et al. 2002). By assuming that subsurface ice exists in the Elysium–Utopia region and that Martian basaltic lavas could act in the same way as terrestrial granite drift, the ice could have survived over 1.3 billion years. The age is close to 1.66 Ga, which corresponds to the recent resurfacing events of the Elysium-derived lava flows (Werner et al. 2011). If water ice was present when the resurfacing of lava flows occurred, it could still exist within the VBF today.

However, the study of the VBF materials in Amazonis Planitia, 4000 km away from our study region, showed that VBF has a loss tangent of 0.005–0.012, which is consistent with dry, moderate-density sediments (Campbell et al. 2008). Our results suggest that water ice possibly exists within the upper few meters of the VBF in the Elysium–Utopia region. The different interpretations could be due to the different geological processes. One obvious difference is the buried depth of the VBF unit. In the Elysium–Utopia region, VBF materials are covered by lava flows to an average depth of ~ 40 m, whereas the VBF materials in Amazonis Planitia are much closer to the surface based on SHARAD observations (Campbell et al. 2008). In addition, the surface morphology and flow-like features in Syria Planum, Amazonis Planitia, and Acidalia Planitia suggest that the VBF in Utopia and Acidalia Planitia represents a possible reservoir of water or mud but have different implications in Amazonis Planitia (Ivanov et al. 2015).

5. Conclusions

The permittivity value of the subsurface layer in the Elysium–Utopia region could provide a hint of the existence of subsurface water ice other than morphological evidence.

Therefore, we developed a method based on the loss tangent to estimate the permittivity of the underlying layer in this paper.

The values of permittivity and loss tangent indicate that the surface materials are dense basaltic lava flows, and the shallow subsurface reflections observed by SHARAD are caused by the interface between lava flows that erupted in different periods. The deep reflections indicate the interface between lava flows and VBF. The value of $\epsilon'_{VBF} = 2.6 \pm 0.9$ derived from the method represents the estimation for the first few meters in depth of the VBF unit. Analysis based on the three-phase power relation suggests that the VBF or its upper few meters may contain more than 10% volume fraction of water ice, but the possibility of a layer of dry and low-density deposits lying beneath the lava flows could not be ruled out. One of the candidate landing sites for first Chinese Martian mission is close to the study region (Wang 2018). Ground-penetrating radar on board the Martian rover of this mission has a working frequency of 35–75 MHz with a potential penetrating capability of several tens of meters (Zhou et al. 2016; Meng et al. 2020). The investigation of in situ radar instruments in the nearby region could help to test our hypothesis. Finally, the proposed method can be used to calculate the permittivity of the underlying layers, which is helpful for understanding the geology and climate evolution of Mars.

SHARAD, CTX, and MOLA data are publicly available on NASA’s Planetary Data System (PDS) website (<http://pds-geosciences.wustl.edu/>). Clutter simulations are available via CO-SHARPS Processing Boutique (<http://www.psi.edu/SHARAD>). We thank the entire SHARAD team for their efforts in acquiring these data and thank the CO-SHARPS teams for the processing boutique. This work was supported by the Science and Technology Development Fund of Macau, Macau SAR (File No. 0089/2018/A3, 121/2017/A3, 119/2017/A3, and 008/2017/AFJ), Pre-research Project on Civil Aerospace Technologies of CNSA (grant No. D020101), and Natural Science Foundation of China (grant No. 41772050 and 41773063). We thank an anonymous reviewer for suggestions that improved the paper.

Appendix

Transmission in the Mantling Layer

If considering the influence of the transmissivity of radar waves between the mantling layer and the shallow subsurface layer, Equation (3) is reformulated as

$$P_{ss} = P_t \left(\frac{G\lambda}{8\pi(H+z)} \right)^2 (1 - |R_s|^2)^2 (1 - |R_m|^2)^2 \times |R_{ss}|^2 L_{ss} \exp(-2\pi f \tan \delta \tau) \quad (13)$$

where R_m is the reflection coefficient at the interface between layers I and II (Figure 4):

$$R_m = \frac{\sqrt{\epsilon'_m} - \sqrt{\epsilon'_1}}{\sqrt{\epsilon'_m} + \sqrt{\epsilon'_1}}. \quad (14)$$

So, the corrected constant term (K') can be rewritten as

$$K' = \ln \frac{(1 - |R_s|^2)^2 |R_{ss}|^2 (1 - |R_m|^2)^2}{|R_s|^2} \quad (15)$$

In Table 3, the corrected constant term has an average value of 0.2657. Based on Equation (15), we estimate that the permittivity of layer III is 2.9, 2.2, and 1.8 for a mantling

permittivity of 2.5, 3.0, and 3.5, respectively. Assuming that the transmissivity between the mantling layer and shallow subsurface layer is 1, the average estimated permittivity of layer III ranges from 2.0 to 3.3 (Table 4). Comparing with the results, the transmission in the mantling layer would cause a small decrease (~ 0.3) in the estimation of the deep subsurface permittivity.

ORCID iDs

Xu Meng  <https://orcid.org/0000-0003-3254-5681>

Yi Xu  <https://orcid.org/0000-0001-8894-525X>

Long Xiao  <https://orcid.org/0000-0002-5271-8554>

Zhiyong Xiao  <https://orcid.org/0000-0002-5026-6937>

References

- Arvidson, R. E., Gooding, J. L., & Moore, H. J. 1989, *RvGeo*, **27**, 39
- Barlow, N. G. 2006, *M&PS*, **41**, 1425
- Bramson, A. M., Byrne, S., Putzig, N. E., et al. 2015, *GeoRL*, **42**, 6566
- Brouet, Y., Becerra, P., Sabouroux, P., et al. 2019, *Icar*, **321**, 960
- Campbell, B., Carter, L., Phillips, R., et al. 2008, *JGRE*, **113**, E12010
- Campbell, B. A., & Morgan, G. A. 2018, *GeoRL*, **45**, 1759
- Carrier, W. D. 1991, *Physical Properties of the Lunar Surface* (New York: Cambridge Univ. Press)
- Carter, L. M., Campbell, B. A., Holt, J. W., et al. 2009, *GeoRL*, **36**, L23204
- Castaldo, L., Mège, D., Gurgurewicz, J., Orosei, R., & Alberti, G. 2017, *E&PSL*, **462**, 55
- Choudhary, P., Holt, J. W., & Kempf, S. D. 2016, *IGRSL*, **13**, 1285
- Dundas, C. M., Bramson, A. M., Ojha, L., et al. 2018, *Sci*, **359**, 199
- Golombek, M. P., Crumpler, L. S., Grant, J. A., et al. 2006, *JGRE*, **111**, E02S07
- Grant, J. A., Arvidson, R., Bell, J. F., et al. 2004, *Sci*, **305**, 807
- Harmon, J. K., Nolan, M. C., Husmann, D. I., & Campbell, B. A. 2012, *Icar*, **220**, 990
- Haynes, M. S., Chapin, E., & Schroeder, D. M. 2018, *ITGRS*, **56**, 6571
- Head, J. W., Mustard, J. F., Kreslavsky, M. A., et al. 2003, *Natur*, **426**, 797
- Holt, J. W., Peters, M. E., Kempf, S. D., et al. 2006, *JGR*, **111**, E06S24
- Holt, J. W., Safaeinili, A., Plaut, J. J., et al. 2008, *Sci*, **322**, 1235
- Ivanov, M. A., Hiesinger, H., Erkeling, G., & Reiss, D. 2014, *Icar*, **228**, 121
- Ivanov, M. A., Hiesinger, H., Erkeling, G., & Reiss, D. 2015, *Icar*, **248**, 383
- Kreslavsky, M. A., & Head, J. W. 2002, *JGRE*, **107**, 5121
- Lauro, S. E., Mattei, E., Pettinelli, E., et al. 2010, *GeoRL*, **37**, L14201
- Lauro, S. E., Mattei, E., Soldovieri, F., et al. 2012, *Icar*, **219**, 458
- Mangold, N., Ansan, V., Masson, P., et al. 2009, *Géomorphologie*, **1**, 23
- Marchant, D. R., Lewis, A. R., Phillips, W. M., et al. 2002, *GSAB*, **114**, 718
- Meng, X., Xu, Y., Xiao, L., et al. 2020, *Icar*, **338**, 113576
- Moore, H. J., Hutton, R. E., Clow, G. D., & Spitzer, C. R. 1987, *Physical Properties of the Surface Materials at the Viking Landing Sites on Mars*, USGS Numbered Series, Report, 1389, <http://pubs.er.usgs.gov/publication/pp1389>
- Morgan, G. A., Campbell, B. A., Carter, L. M., & Plaut, J. J. 2015, *GeoRL*, **42**, 7336
- Mouginot, J., Pommerol, A., Beck, P., Kofman, W., & Clifford, S. M. 2012, *GeoRL*, **39**, L02202
- Mouginot, J., Pommerol, A., Kofman, W., et al. 2010, *Icar*, **210**, 612
- Nunes, D. C. 2012a, AGU Fall Meeting, 2012 P33C-1955
- Nunes, D. C. 2012b, LPSC, **43**, 2233
- Nunes, D. C., Smrekar, S. E., Fisher, B., et al. 2011, *JGRE*, **116**, E04006
- Nunes, D. C., Smrekar, S. E., Safaeinili, A., et al. 2010, *JGRE*, **115**, E10004
- Ody, A., Poulet, F., Bibring, J.-P., et al. 2014, *LPICo*, **1791**, 1191
- Orosei, R., Lauro, S. E., Pettinelli, E., et al. 2018, *Sci*, **361**, 490
- Orosei, R., Rossi, A. P., Cantini, F., et al. 2017, *JGRE*, **122**, 1405
- Picardi, G., Plaut, J. J., Biccari, D., et al. 2005, *Sci*, **310**, 1925
- Plaut, J. J., Picardi, G., Safaeinili, A., et al. 2007, *Sci*, **316**, 92
- Plaut, J. J., Safaeinili, A., Holt, J. W., et al. 2009, *GeoRL*, **36**, L02203
- Porcello, L. J., Jordan, R. L., Zelenka, J. S., et al. 1974, *IIEEP*, **62**, 769
- Ruff, S. W., & Christensen, P. R. 2002, *JGRE*, **107**, 5127
- Russell, P. S., & Head, J. W. 2003, *JGRE*, **108**, 5064
- Sandmeier, K. J. 2012, REFLEXW Version 7.0 Windows™ 9x/NT/2000/XP/7-Program for the Processing of Seismic, Acoustic or Electromagnetic Reflection and Transmission Data, 7, <https://www.sandmeier-geo.de/reflexw.html> (Karsruhe, Germany)
- Selvans, M. M., Plaut, J. J., Aharonson, O., et al. 2010, *JGRE*, **115**, E09003
- Seu, R., Phillips, R. J., Biccari, D., et al. 2007, *JGR*, **112**, E5S05
- Simon, M. N., Carter, L. M., Campbell, B. A., Phillips, R. J., & Mattei, S. 2014, *JGRE*, **119**, 2291
- Smith, D. E., Zuber, M. T., Frey, H. V., et al. 2001, *JGRE*, **106**, 23689
- Stillman, D. E., & Grimm, R. E. 2011, *JGRE*, **116**, E03001
- Stillman, D. E., Grimm, R. E., & Dec, S. F. 2010, *J. Phys. Chem. B.*, **114**, 18
- Stuurman, C. M., Osinski, G. R., Holt, J. W., et al. 2016, *GeoRL*, **43**, 9484
- Tanaka, K. L., Skinner, J. A., Dohm, J. M., et al. 2014, *Geologic Map of Mars*, USGS Scientific Investigations Map, 3392, <http://pubs.er.usgs.gov/publication/sim3292>
- Tanaka, K. L., Skinner, J. A., & Hare, T. M. 2005, *Geologic Map of the Northern Plains of Mars*, USGS Scientific Investigations Map, 2888, <http://pubs.er.usgs.gov/publication/sim2888>
- Ulaby, F. T., Moore, R. K., & Fung, A. K. 1986, *Microwave Remote Sensing: Active and Passive* (Boston, MA: Artech House)
- Vaucher, J., Baratoux, D., Mangold, N., et al. 2009, *Icar*, **204**, 418
- Wang, F. 2018, COPUOS 61, China's Cooperation Plan on Lunar and Deep Space Exploration, 61, <https://www.unoosa.org/documents/pdf/copuos/2018/copuos2018tech19E.pdf> (Vienna, Austria)
- Warner, N. H., Golombek, M. P., Sweeney, J., et al. 2017, *SSRv*, **211**, 147
- Watters, T. R., Leuschen, C. J., Campbell, B. A., et al. 2017, *GeoRL*, **44**, 9208
- Werner, S. C. 2009, *Icar*, **201**, 44
- Werner, S. C., Tanaka, K. L., & Skinner, J. A. 2011, *P&SS*, **59**, 1143
- Zhou, B., Shen, S. X., Ji, Y. C., et al. 2016, in 16th Int. Conf. Ground Penetrating Radar (GPR), The Subsurface Penetrating Radar on the Rover of China's Mars 2020 Mission (Piscataway, NJ: IEEE), 1